Thin Film TaFe, TaCo, and TaNi as Potential Optical Hydrogen Sensing Materials

Bannenberg, L.J.; Veeneman, E.M.; Straus, F.I.B.; Chen, H.Y.; Kinane, Christy J. ; Hall, Stephen; Thijs, M.A.; Schreuders, H.

DOI
10.1021/acsomega.4c06955

Publication date
2024

Document Version
Final published version

Published in
ACS Omega

ACS OMEGA

Open Access

http://pubs.acs.org/journal/acsodf

Article

Thin Film TaFe, TaCo, and TaNi as Potential Optical Hydrogen Sensing Materials

Lars J. Bannenberg,* Isa M. Veeneman, Folkert I. B. Straus, Hsin-Yu Chen, Christy J. Kinane, Stephen Hall, Michel A. Thijs, and Herman Schreuders

Cite This: *ACS Omega* 2024, 9, 41978−41989

Read Online

ACCESS | Metrics & More | Article Recommendations | Supporting Information

ABSTRACT: This paper studies the structural and optical properties of tantalum−iron-, tantalum−cobalt-, and tantalum−nickel-sputtered thin films both ex situ and while being exposed to various hydrogen pressures/concentrations, with a focus on optical hydrogen sensing applications. Optical hydrogen sensors require sensing materials that absorb hydrogen when exposed to a hydrogen-containing environment. In turn, the absorption of hydrogen causes a change in the optical properties that can be used to create a sensor. Here, we take tantalum as a starting material and alloy it with Fe, Co, or Ni with the aim to tune the optical hydrogen sensing properties. The rationale is that alloying with a smaller element would compress the unit cell, reduce the amount of hydrogen absorbed, and shift the pressure composition isotherm to higher pressures. X-ray diffraction shows that no lattice compression is realized for the crystalline Ta body-centered cubic phase when Ta is alloyed with Fe, Co, or Ni, but that phase segregation occurs where the crystalline body-centered cubic phase coexists with another phase, as for example an X-ray amorphous one or fine-grained intermetallic compounds. The fraction of this phase increases with increasing alloyant concentration up until the point that no more body-centered cubic phase is observed for 20% alloyant concentration. Neutron reflectometry indicates only a limited reduction of the hydrogen content with alloying. As such, the ability to tune the sensing performance of these materials by alloying with Fe, Co, and/or Ni is relatively small and less effective than substitution with previously studied Pd or Ru, which do allow for a tuning of the size of the unit cell, and consequently tunable hydrogen sensing properties. Despite this, optical transmission measurements show that a reversible, stable, and hysteresis-free optical response to hydrogen is achieved over a wide range of hydrogen pressures/concentrations for Ta−Fe, Ta−Co, or Ta−Ni alloys which would allow them to be used in optical hydrogen sensors.

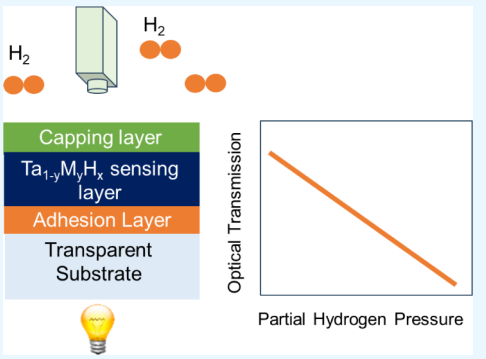

1. INTRODUCTION

Hydrogen sensors are pivotal in a future hydrogen economy, as the use of hydrogen comes with safety hazards because hydrogen−air mixtures can be flammable or even explosive. On top of that hydrogen leaks should also be detected and minimized as hydrogen has been identified as an indirect green house gas.[1−7] Optical hydrogen sensors are particularly well-suited to sense hydrogen as they have a large and reversible hydrogen sensing range, can be made small and inexpensive, and most of all do not require any electric currents near the sensing area, making them inherently safe. At the heart of an optical hydrogen sensor is an optical hydrogen sensing material. When exposed to a hydrogen-containing environment, the optical hydrogen sensing material, typically a metal hydride, absorbs hydrogen, in turn changing its optical properties. These optical properties can then be probed by e.g., measuring the optical reflectivity or transmission of the material, which then is directly related to the hydrogen concentration around the sensor.[8−14]

The ideal optical hydrogen sensor material should feature a large sensing range, high sensitivity, and a fast, reversible, and hysteresis-free response. A hysteresis-free response is important as it ensures that the sensor always gives the same response irrespective of the hydrogen pressure/concentration history to which the sensor has been exposed to. If the hydrogen-to-metal ratio of the sensing material is different for increasing and decreasing hydrogen pressures, such as when a first-order phase transition occurs upon hydrogen absorption, hysteresis will also be observed in the sensor's output. As such, one optical transmission value can then correspond to at least two hydrogen concentrations, and the hydrogen concentration cannot be uniquely determined. Therefore, to achieve a large sensing range and hysteresis-free response, the optical hydrogen sensing material should gradually absorb hydrogen upon increasing partial hydrogen pressure/concentration

Received: July 29, 2024
Revised: August 26, 2024
Accepted: August 27, 2024
Published: September 26, 2024

without undergoing a phase transition upon hydrogen absorption (i.e., a large-solid solution range of hydrogen and the host metal). On top of that, plastic deformation, another source of hysteresis, should also be minimized.[15−19] Indeed, if the material deforms plastically, additional mechanical work is needed to accommodate the hydrogen, which shifts the pressure/concentration at which hydrogen is absorbed to a higher value than the pressure/concentration at which the hydrogen is released. Furthermore, a fast response can be achieved by selecting a material with high hydrogen diffusivity as well as by reducing the total amount of hydrogen that is absorbed.

In the literature, palladium and its alloys[20−30] have been considered extensively as hydrogen sensing materials, as well as hafnium-[31,32] and magnesium-based alloys have also been considered for switchable optical mirrors.[33−36] More recently, tantalum-based hydrogen sensing materials have been developed as hysteresis-free and versatile hydrogen sensing materials.[37−40] When tantalum-based materials are combined with a suitable capping layer that promotes hydrogen dissociation and prevents oxidation,[41] these materials provide a sensing range of over 7 orders of magnitude in hydrogen pressure/concentration that is free of any hysteresis. The absence of hysteresis is due to the large solid solubility range of hydrogen and tantalum. Whereas in bulk tantalum, a series of phase transitions are observed when it absorbs hydrogen,[42] nanoconfinement in clamped thin films effectively suppresses these phase transitions.[39]

Alloying is an effective way to tune the hydrogen sensing properties of tantalum. It can shift the sensing range and reduce the amount of hydrogen that is absorbed to reduce the response times. Indeed, at room temperature tantalum already absorbs significant amounts of hydrogen below the ppb concentration level ($\approx TaH_{0.5}$) which is not relevant for most applications but increases the response time. Indeed, the fact that hydrogen is already absorbed at such low hydrogen concentrations does not contribute to the sensitivity of the hydrogen sensor in the concentration range that is important, while it does result in a large amount of hydrogen that needs to be dissociated and transported, slowing down kinetics and an increased volumetric expansion when the material is exposed to hydrogen, which ultimately may compromise the stability and lifetime of the sensor. Therefore, it is beneficial to shift the pressure range to higher hydrogen concentrations while preserving the hysteresis-free and highly sensitive response of tantalum.

So far, palladium and ruthenium have been considered successful alloyants. These elements both crystallize in a cubic structure and form a solid solution up to $y = 0.12$ for Pd and at least $y = 0.3$ for Ru in thin film $Ta_{1-y}M_y$.[38,40] Importantly, both palladium (0.015 nm^3) and ruthenium (0.014 nm^3) have a volume per atom substantially smaller than that of tantalum (0.018 nm^3). Alloying with a smaller unit cell than Ta results in compressive strain, which in turn reduces the enthalpy of hydrogenation, and thus reduces the amount of hydrogen absorbed by the layer at low hydrogen pressures.[43] Indeed, the results show a shift of the pressure range to higher hydrogen concentrations/pressures, while the enthalpy of hydrogenation becomes less favorable.

To shift the pressure range, it might be more effective to use elements with an even smaller volume per unit cell but with a compatible crystal structure. In this light, iron, cobalt, and nickel can be considered as attractive candidates: they have a cubic unit cell with a substantially smaller volume per atom of 0.012, 0.011, and 0.011 nm^3 for Fe, Co, and Ni, respectively. However, the concentration range over which a solid solution is formed in the bulk is reported to be moderate: up to $y \approx 0.1$ (Fe), 0.2 (Co), and 0.2 (Ni) at high temperatures and substantially smaller at lower temperatures and previously studied Ru. Above these solubility limits, intermetallic compounds may be formed.[44−51] However, these solubility limits are in most cases estimated on the basis of thermodynamic simulations, and experimental studies of the Ta-rich alloys with Fe, Co, or Ni are rare. Furthermore, the structure of sputtered thin films may deviate substantially from the bulk, in part due to the high kinetic energy of the atoms during the deposition (i.e., effectively a high temperature).

The purpose of this paper is to synthesize and study the structural and optical transmission of 40 nm Ta−Fe, Ta−Co, and Ta−Ni alloy thin films with $0.0 \leq y \leq 0.2$ when exposed to hydrogen to identify whether these materials are suitable for optical hydrogen sensing applications. In particular, the question is whether substitution of Ta by Fe, Co, and Ni allows tuning of the sensing response. The Ta-based thin films are capped with a 10 nm $Pd_{0.6}Au_{0.35}Cu_{0.05}$ capping layer to prevent oxidation and promote the dissociation of hydrogen.[41] First, we show using X-ray diffraction that for Ta−Fe, Ta−Co, and Ta−Ni, the films consist of at least two phases: one crystalline α $Ta_{1-y}M_y$ phase and another phase, as for example an X-ray amorphous one and/or fine-grained intermetallic compounds, of which the fraction increases with increasing concentration of the alloyant, until at $y = 0.2$ and no bcc phase is observed. Neutron reflectometry indicates that for a given hydrogen pressure/concentration alloying reduces the hydrogen concentration in the $Ta_{1-y}M_yH_x$ layer and the layer expansion, but limited to a much smaller extent than for, e.g., doping by Ru. Optical measurements indicate a hysteresis-free response for alloys across 7 orders of magnitude in hydrogen pressure/concentration for all compounds with $y < 0.15$. As such, while these alloys can be used for optical hydrogen sensing, alloying tantalum with Fe, Co, or Ni provides less flexibility to tune the hydrogen sensing properties than Pd or Ru.

2. EXPERIMENTAL SECTION

2.1. Sample Fabrication. All samples consist of a 4 nm titanium adhesion layer, a 40 nm $Ta_{1-y}M_y$ (M = Fe, Co or Ni) sensing layer, and a 10 nm capping layer made of $Pd_{0.6}Au_{0.35}Cu_{0.05}$ to catalyze the hydrogen dissociation and recombination reaction and prevent the film from oxidation (nominal thicknesses). The Ti layer functions also as a seed layer to induce the bcc α phase.[52−56] A thickness of 40 nm is chosen for the sensing layer, as it is thick enough to provide sufficient optical contrast in transmission when it is exposed to hydrogen but thin enough to have a sufficient absolute optical transmission that can be detected. For the capping layer, 10 nm is chosen to ensure that we have a coherent layer, although we note that this is also the case when we would have chosen a 5 nm thick layer. These are also the same thicknesses as those considered in our earlier works, which facilitates comparison. The reason to select $Pd_{0.6}Au_{0.35}Cu_{0.05}$ instead of pure Pd is that the introduction of gold into the capping layer accelerates the hydrogen dissociation while Cu makes the alloy less susceptible to CO poisoning.[26,41] These layers are deposited on 10 × 10 mm^2 quartz substrates, which were used with a thickness of 0.5 mm and surface roughness <0.4 nm (Mateck

https://doi.org/10.1021/acsomega.4c06955
ACS Omega 2024, 9, 41978−41989

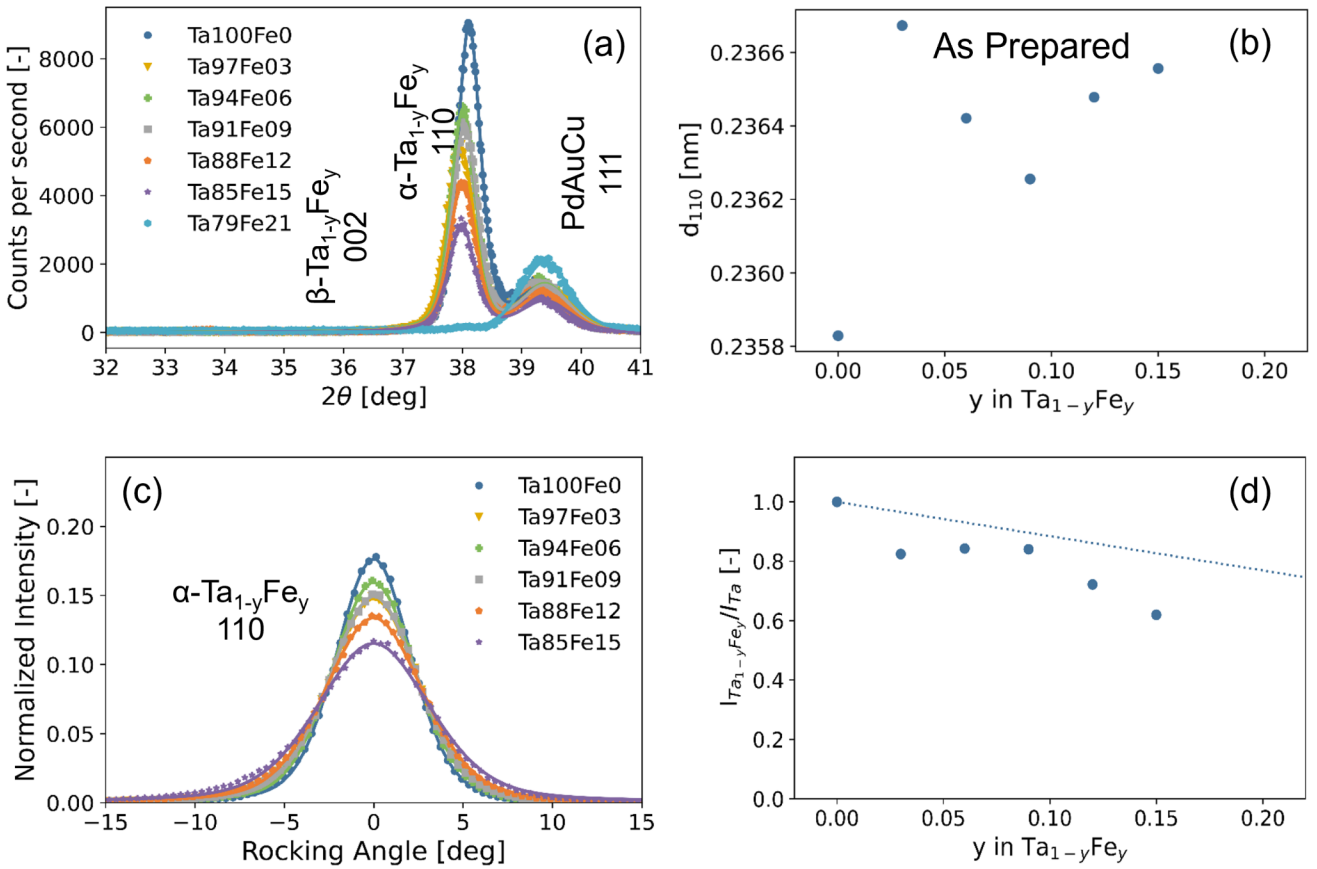

Figure 1. Ex situ X-ray diffraction (XRD) results of the 40 nm $Ta_{1-y}Fe_y$ thin films with a 4 nm Ti adhesion layer capped with a 10 nm $Pd_{0.6}Au_{0.35}Cu_{0.05}$ layer before exposure of the thin films to hydrogen and measured in air. (a) Diffraction patterns (Cu Kα, λ = 0.1542 nm) of the $Ta_{1-y}Fe_y$ thin films. The continuous lines represent fits of two pseudo-Voigt functions to the experimental data accounting for the bcc ⟨110⟩ $Ta_{1-y}Fe_y$ and fcc ⟨111⟩ $Pd_{0.6}Au_{0.35}Cu_{0.05}$ peaks. (b) Fe doping dependence of the d_{110} spacing in $Ta_{1-y}Fe_y$. (c) Rocking curves of the $Ta_{1-y}Fe_y$ thin films around the bcc $Ta_{1-y}Fe_y$⟨110⟩ peak. (d) Fe concentration dependence of the total intensity of the ⟨110⟩ diffraction peak in $Ta_{1-y}Fe_y$, in which the effects of both the changing amplitude and width are incorporated. It is computed by multiplying the integrated intensity of the fitted ⟨110⟩ $Ta_{1-y}Fe_y$ peak by the fwhm of the rocking curve of (b). The intensity is subsequently scaled to the intensity of the Ta sample. The dashed line indicates the theoretically expected Fe concentration dependence of the intensity according to eq 2.

GmbH, Jülich, Germany) for the X-ray diffraction, X-ray reflectometry, and optical measurements. Larger fused quartz substrates were used for the neutron reflectometry measurements. These substrates have a diameter of 76.2 mm (3 in.) with a thickness of 3.0 mm, a surface roughness <0.5 nm and a flatness of 2 λ that is guaranteed over 85% of the central surface. It implies that the maximum peak−valley distance on the central surface is 2 × 633 nm ≈1.3 μm (Coresix Precision Glass, Inc., VA, United States of America).

All layers are produced by magnetron sputtering in 0.3 Pa of Ar in an ultrahigh vacuum chamber (AJA Int.) with a base pressure of $p < 10^{-6}$ Pa. Typical deposition conditions include 125 W DC for Ta at about 0.15 nm s^{-1}, 8−28 W DC for Fe, 7−24 W DC for Co, 4−19 W DC for Ni, 0.05 nm s^{-1} (100 W DC) for Ti and 0.18 nm s^{-1} (50 W DC) for the custom-made $Pd_{0.6}Au_{0.35}Cu_{0.05}$ alloy target. The exact sputter times and powers can be found in Table S1. All targets have a diameter of 5.08 mm (2 in.) and a purity of at least 99.9% (Mateck GmbH, Jülich, Germany). To determine the deposition rates, each target was sputtered independently at a fixed power for a well-defined time. Next, the sample was measured by X-ray reflectometry (XRR) to obtain the layer thickness of this reference sample on the basis of which we computed the sputter rate. Nitridation and oxidation of the Ta layers was prevented by presputtering the Ta target for 60 min and stored in an Ar-filled glovebox.

X-ray diffraction (XRD) and reflectometry (XRR) was used to verify the crystal structure and thicknesses of all samples (see below for experimental details). The analysis of the XRR data reveals that the layer thickness deviates by no more than 5% or 1 nm, the density of the various layers is consistent with the literature value for bulk material, and the root-mean-square roughness of the various layers is at a maximum of 2 nm (Figure S1).

Before the measurements commenced, all samples were exposed to three cycles of hydrogen with a maximum pressure of $P_{H2} = 10^6$ Pa at T = 28 °C. Reproducible and hysteresis-free results are already obtained from the second cycle onward. Differences between the first and subsequent cycles are often observed for thin film metal hydrides. These differences arise from the settling of the microstructure, and also in this case, we observe that the d-spacing is reduced and the preferred orientation of the $Ta_{1-y}M_y$ layers is improved and the preferred orientation improves (Figures 1 and S2 for Fe, Figures S3, S4, and S5 for Co, and Figures S6, S7, and S8 for Ni).

2.2. Structural Measurements. All X-ray diffraction and reflectometry measurements were performed with a Bruker D8 Discover instrument (Cu Kα, λ = 0.1542 nm). This

https://doi.org/10.1021/acsomega.4c06955
ACS Omega 2024, 9, 41978−41989

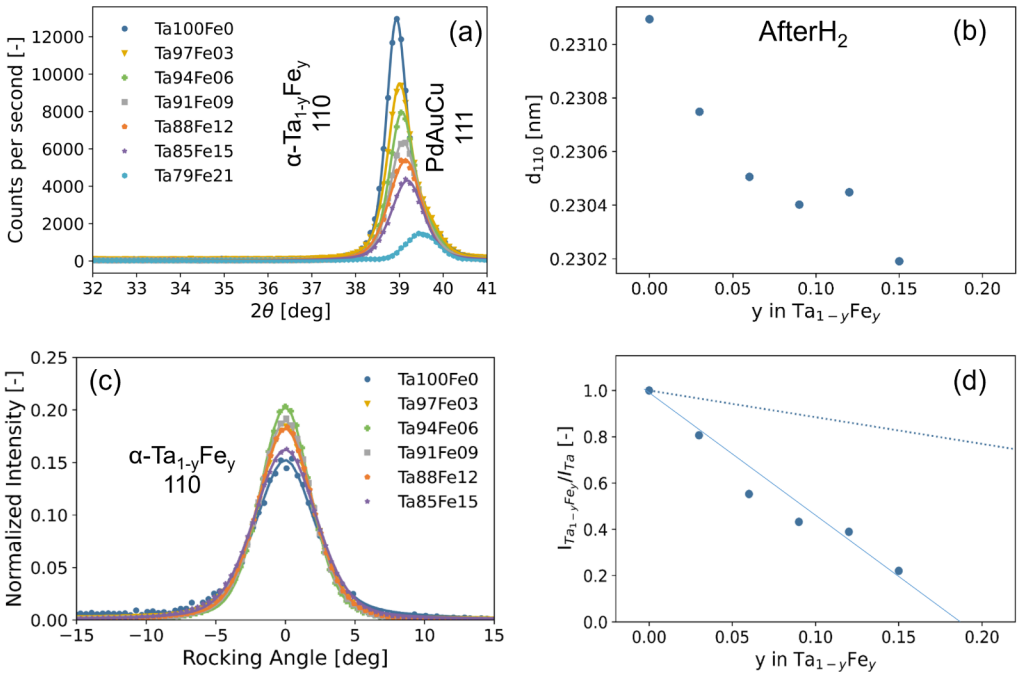

Figure 2. Ex situ X-ray diffraction (XRD) results of the 40 nm $Ta_{1-y}Fe_y$ thin films with a 4 nm Ti adhesion layer and a 10 nm $Pd_{0.6}Au_{0.35}Cu_{0.05}$ capping layer after exposure to hydrogen and measured in air. (a) Diffraction patterns (Cu Kα, λ = 0.1542 nm) of the $Ta_{1-y}Fe_y$ thin films. The continuous lines represent fits of two pseudo-Voigt functions to the experimental data to account for the bcc(110) $Ta_{1-y}Fe_y$ and fcc(111) $Pd_{0.6}Au_{0.35}Cu_{0.05}$ peaks. (b) Fe concentration dependence of the d_{110} spacing in $Ta_{1-y}Fe_y$. The continuous line is an ordinary least-squares fit to the data. (c) Rocking curves of the $Ta_{1-y}Fe_y$ thin films around the bcc $Ta_{1-y}Fe_y$(110) peak. In this figure, the intensity is normalized to the integrated intensity across all rocking angles. (d) Fe concentration dependence of the total intensity of the (110) diffraction peak in $Ta_{1-y}Fe_y$ by taking into account the effect of both the changing amplitude and width. The intensity is computed by multiplying the integrated intensity of the fitted (110) $Ta_{1-y}Fe_y$ peak by the fwhm of the rocking curve of (b). The intensity is subsequently scaled to the intensity of the Ta sample. The continuous line indicates an ordinary least-square fit to the data and the dashed line indicates the theoretically expected Fe concentration dependence of the intensity according to eq 2.

diffractometer is equipped with a Göbel mirror and a LYNXEYE XE detector (Bruker AXS GmbH, Karlsruhe, Germany). The XRD measurements were performed with a 0.6 mm fixed slit on the primary and two 0.6 mm slits on the secondary side with the detector operated in 0D mode. For the XRR measurements 0.1 mm fixed slits were used. To avoid saturation of the detector, $0 < 2\theta < 2°$ was measured with a 0.1 mm Cu foil attenuator, and stitched to the $1 < 2\theta < 4°$ using a home-written Python code. The data were fitted with GenX3[57] to obtain estimates for the layer thickness, roughness and density of the thin films.

In situ neutron reflectometry measurements were performed using the time-of-flight neutron reflectometers ROG and OFFSPEC. The ROG is located at the 2.3 MW HOR reactor in the Delft University of Technology, Delft, The Netherlands; whereas OFFSPEC is located at the ISIS pulsed neutron source, Didcot, United Kingdom.[58]

During the measurements at the ROG, the double disc chopper was set to a frequency of 17.7 Hz with an interdisc distance of 0.280 m, the incident angle to 8.5 mrad, and the first and second slit to 1.2 and 0.6 mm, respectively. The spectrum between $0.11 < \lambda < 1.0$ nm was used. These settings result in a wavelength resolution of $\Delta\lambda/\lambda \approx 2.5\%$, a Q-range of $0.11 < Q < 0.98$ nm^{-1}, a footprint of $65/80 \times 40$ mm^2 (umbra/penumbra) and a resolution of $\Delta Q/Q \approx 5\%$. The neutrons were detected by using a ^{3}He detector. The measurements at OFFSPEC were performed with an incident angle of 11 mrad and with a vertical slit opening of 4.184 and 0.5025 mm for the first and second slit, respectively. This resulted in a Q-range of $0.1 < Q < 0.84$ nm^{-1}, a footprint of $44/75 \times 30$ mm^2 umbra/penumbra and a resolution of $\Delta Q/Q \approx 0.04\%$. The neutrons were detected using a position sensitive wavelength shifting fiber scintillator detector.

The samples were hydrogenated at T = 22 °C inside a temperature- and pressure-controlled cell as described elsewhere.[59] To vary the partial hydrogen pressure, the absolute pressure of gas mixtures of 0.1% or 4.0% H_2 in Ar gas was changed stepwise between 1.5 mbar and 6.1 bar ($\Delta c_{H2}/c_{H2} <$ 2%, Linde Gas Benelux BV, Dieren, The Netherlands).

All data were fitted with GenX3[57,60] providing estimates for the layer thickness, roughness, and scattering length density (SLD) for all three layers. Since we are predominately interested in the thickness and SLD of the $Ta_{1-y}M_y$ layer and owing to a high correlation between the thickness of the $Ta_{1-y}M_y$ and $Pd_{0.6}Au_{0.35}Cu_{0.05}$ layers, we fixed the thickness of the Ti and $Pd_{0.6}Au_{0.35}Cu_{0.05}$ film to the value of the as-prepared sample. As 10 nm $Pd_{0.6}Au_{0.35}Cu_{0.05}$ also expands slightly, this approach results in a small overestimation of the layer expansion of the $Ta_{1-y}M_y$ layer. From the fitted parameters, we can deduce the hydrogen concentration x of the layer using

$$x = \left(\frac{\mathrm{SLD}_{\mathrm{Ta}_{1-y}M_yH_x}}{\mathrm{SLD}_{\mathrm{Ta}_{1-y}M_y}} \frac{d_{\mathrm{Ta}_{1-y}M_yH_x}}{d_{\mathrm{Ta}_{1-y}M_y}} - 1 \right) \frac{(1-y)b_{\mathrm{Ta}} + yb_M}{b_{\mathrm{H}}} \tag{1}$$

with $SLD = \sum_{i=1}^{N} b_i N_i$ is the SLD of the layer; b_{Ta} = 6.91 fm, b_{Fe} = 9.45 fm, b_{Co} = 2.49 fm, b_{Ni} = 10.3 fm, and b_H = −3.739 fm are the scattering lengths of tantalum, iron, cobalt, nickel,

https://doi.org/10.1021/acsomega.4c06955
ACS Omega 2024, 9, 41978−41989

and hydrogen, respectively;[61] and N_i is the number of atoms i per volume unit.[62] The χ^2 values of the fits vary between 1.1 and 1.6. Atomic force microscopy (AFM) measurements were performed with a Bruker Multimode AFM in tapping mode.

2.3. Optical Measurements. Hydrogenography was used to measure the optical transmission.[63] This setup is equipped with five Philips MR16 MASTER LEDs (10/50 W) with a color temperature of 4000 K as a light source (Figure S9) and an imaging source DFK 23UM021 1/3 "Aptina CMOS MT9M021 1280 × 960 pixels^2 color camera with an Edmunds Optics 55-906 lens. A 750 nm low-pass wavelength filter is used in front of the lens. The camera records the red, green, and blue domains separately, and the wavelength-dependent sensitivity of each of these channels is provided in Figure S10. From the raw camera images, we averaged the transmission over an area of approximately 80 mm^2 corresponding to roughly 100 × 100 pixels^2. A reference sample that does not hydrogenate is used to compensate for fluctuations of the light source and account for the response of the 10 nm $Pd_{0.60}Au_{0.40}$ capping layer. The partial hydrogen pressures were varied between $10^{-1} < P_{H2} < 10^{6}$ Pa by using 0.10%, 4.0% in Ar gas mixtures ($\Delta c_{H2}/c_{H2} < 2\%$, Linde Gas Benelux BV, Dieren, The Netherlands) and 100% H_2 and changing the total pressure inside the sample chamber between $0.15 < P_{tot} < 1.0 \times 10^{6}$ Pa. Typical gas flows are 20 sccm for increasing pressure steps and 100 sccm for decreasing pressure steps.

3. RESULTS

3.1. Structural Behavior. *3.1.1. Ex Situ X-Ray Diffraction.* As a first step, we study how the substitution of Ta with Fe, Co, and Ni affects the structural properties of the thin film materials. Most importantly, we focus on whether: (i) a solid solution is formed between Ta and the alloyant and (ii) there is no phase coexistence. This is important, as in this way the favorable hydrogen sensing properties are likely retained, while the alloying allows one to tune the hydrogen sensing range. In the main text, we focus on the result of substituting Ta with Fe. Additional results on substitution of Ta with Co and Ni are reported in the Supporting Information.

Figures 1 and 2 present X-ray diffraction (XRD) measurements of the $Ta_{1-y}Fe_y$ based thin films, before and after exposure to hydrogen, respectively. Both sets of measurements show qualitatively similar results. For the $Ta_{1-y}Fe_y$ layer, only the 110 bcc α Ta peak is observed, implying a strong texture of this layer with the ⟨110⟩ direction pointing out-of-plane. For the $Pd_{0.6}Au_{0.35}Cu_{0.05}$ layer, which has an fcc structure, we observed the ⟨111⟩ diffraction peak. The intensity of this peak varies with Fe concentration as the mosaicity of this layer is affected by the layer underneath. No additional diffraction peaks are observed for any of the compositions (see also Figure S2 for the full diffraction patterns). Comparing the XRD measurements before (1) and after (2) exposure to hydrogen, we observe that the lattice contracts substantially after exposure to hydrogen, which is often observed for metal hydrides after exposure to hydrogen. Furthermore, comparing the rocking scans, we see that the preferential orientation of the film improves and that the fraction of the α phase decreases. This settling of the microstructure of thin film metal hydrides is irreversible and often seen after the first exposure to hydrogen (see, e.g.,[28,64]

Most importantly, two important conclusions can be derived from Figures 1 and 2. First, we observe that the (110) bcc α-Ta peak position is hardly affected by the substitution of Ta by Fe. This is reflected in the d_{110} spacing [Figure 2b], which is only changed by a maximum value of 0.3%. This is strikingly different from similar amounts of substitution of Ta by Ru (3%).[40] In fact, one would expect a much larger lattice suppression of about 7% based on Vergard's law for $y = 0.2$. It suggests that the Fe substitution is not effective in reducing the lattice constant of bcc α-Ta for sputtered thin films.

Furthermore, we observe a sharp decline of the intensity of the 110 bcc α-Ta peak until the point where no (110) bcc α-Ta peak can be discerned for $y = 0.21$. While a small decrease is expected due to a reduction of the total amount of electrons in the material that diffract the X-rays, such a reduction may also be due to a less perfect preferential orientation or indicate the formation of other phases in the material. To analyze whether preferential orientation plays a role, we performed rocking scans at the (110) bcc α-Ta peak position. In such a rocking scan, the diffraction angle is kept constant while the direction of the film that is probed changes and is no longer out-of-plane (i.e., the momentum transfer vector changes in direction but not in magnitude). The results, displayed in Figure 2c show that there are small changes in the degree of preferential orientation, but that these changes are too small to explain the dramatic decrease in peak amplitude.

As a next step, we calculate the total peak intensity by taking into account the effect of preferential orientation. We report this in Figure 2d alongside an (i) ordinary least-square fit of the data to a linear function and (ii) the theoretically expected decrease in peak intensity for a solid solution of Ta and Fe. For this, we expect a decreasing intensity, as a replacement of Ta ($Z = 73$) by Fe ($Z = 26$) reduces for a bcc structure the fraction of X-rays diffracted by the material according to

$$\begin{aligned} I_{hkl} &\propto |F_{hkl}|^2 \\ &= \left| \sum_i^N f_j(\lambda, \theta) \exp\left[2\pi i(hx_j + ky_j + lz_j)\right] \right|^2 \\ &\propto Z^2 \\ &= [(1-y)Z_{Ta} + yZ_{Fe}]^2 \\ &= [(1-y)73 + y26]^2 \end{aligned} \tag{2}$$

with F_{hkl} as the structure factor, N and $x_j y_j z_j$ as the number and relative coordinates of the atoms in the primitive (bcc) unit cell and $f_j(\lambda,\theta)$ the form factor that can be approximated as $f_j(\lambda, \theta) \approx Zr_e g(\theta, \lambda)$. We observe that the deduced decrease in the peak intensity is much larger than the theoretically expected one. As such, additional phases are formed. There could be various possibilities for one or more phases being formed. Following the Ta−Fe phase diagrams, it is possible that intermetallic compounds are formed.[47−51] Furthermore, it could also be that an X-ray amorphous phase is formed or a combination of the two. For all options, we cannot find conclusive evidence. In the out-of plane diffraction patterns we do not observe any other diffraction peak that is not related to either fcc-$Pd_{0.6}Au_{0.35}Cu_{0.05}$ or bcc-Ta, while additional in-plane X-ray diffraction measurements (Figures S11−S13) also do not reveal the presence of an crystalline additional phase. In addition, AFM measurements show that the morphology of the surface of the $Ta_{0.79}Fe_{0.21}$ surface is substantially different (Figure S14). Whereas, the Ta surface is completely smooth with a low roughness, there are regions on

https://doi.org/10.1021/acsomega.4c06955
ACS Omega 2024, 9, 41978−41989

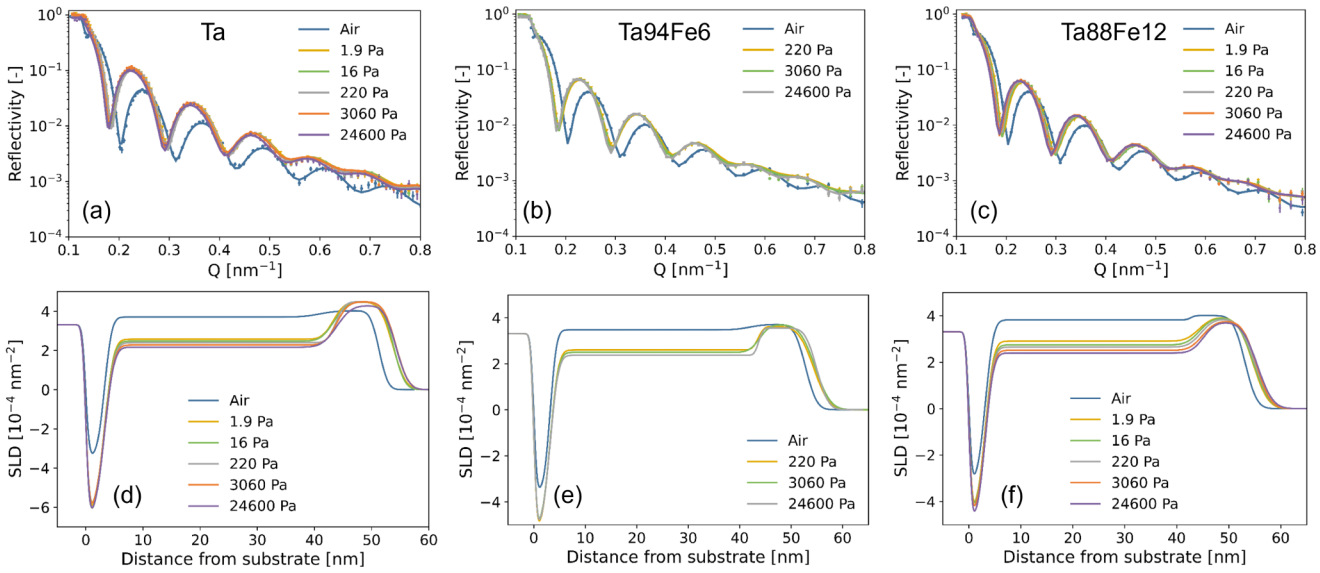

Figure 3. In situ NR results of the 40 nm $Ta_{1-y}Fe_y$ thin films with a 4 nm Ti adhesion layer and capped with 10 nm $Pd_{0.6}Au_{0.35}Cu_{0.05}$ at T = 22 °C. (a−c) Reflectograms of the $Ta_{1-y}Fe_y$ thin films with (a) y = 0, (b) y = 0.06, and (c) y = 0.12 measured for the hydrogen pressures indicated in the legend and for increasing pressure steps. The continuous lines represent the fits of a model to the data, on the basis of which estimates for the scattering length density and layer thickness are obtained (see Figure 4). (d−f) Scattering length density (SLD) profiles for (d) y = 0, (e) y = 0.06, and (f) y = 0.12.

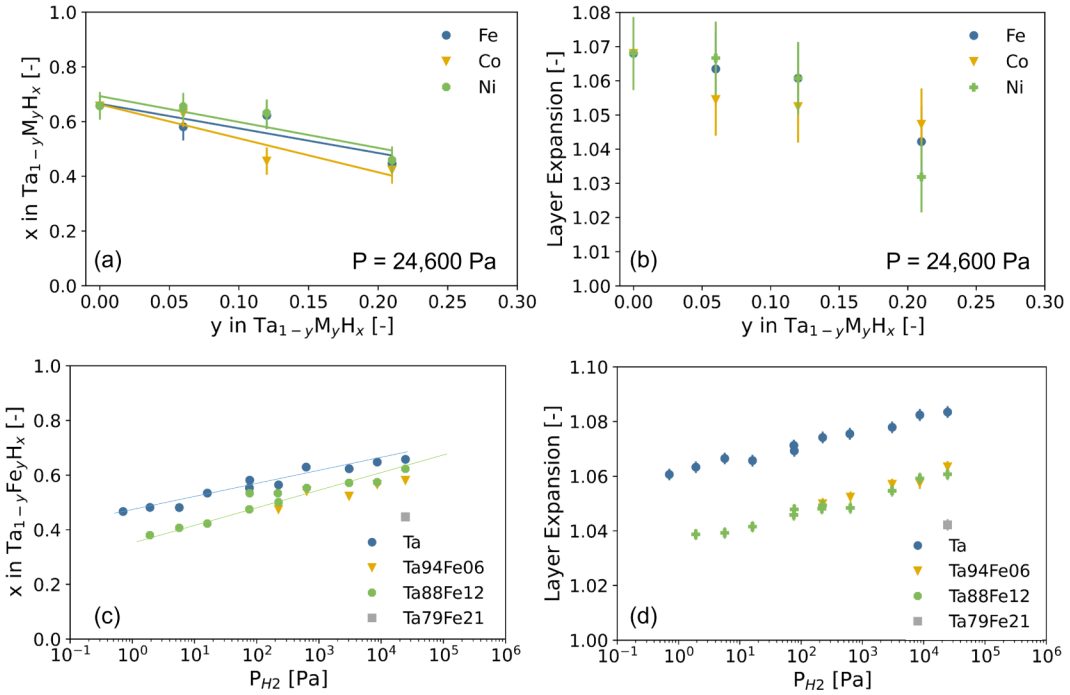

Figure 4. In situ NR results of the 40 nm $Ta_{1-y}Fe_y$, $Ta_{1-y}Co_y$, and $Ta_{1-y}Ni_y$ thin films with a 4 nm Ti adhesion layer and capped with 10 nm $Pd_{0.6}Au_{0.35}Cu_{0.05}$ at T = 22 °C. A selection of the data with the corresponding fits and SLD profiles can be found in Figures 3 and S15. (a) Fe/Co/Ni concentration dependence of the amount of hydrogen absorbed by the $Ta_{1-y}M_yH_x$ layer at P_{H2} = 24600 Pa. (b) Fe/Co/Ni concentration dependence of the relative layer expansion of the $Ta_{1-y}M_yH_x$ layer at P_{H2} = 24600 Pa. (c) Hydrogen pressure dependence of the amount of hydrogen absorbed by the $Ta_{1-y}Fe_yH_x$ layer. (d) Hydrogen pressure dependence of the expansion of the $Ta_{1-y}Fe_y$ layer. The lines are an ordinary least-squares fit to the data.

the $Ta_{0.79}Fe_{0.21}$ surface that are substantially higher, which may point toward that the material is not completely homogeneous and that phase separation may occur. Nevertheless, the fraction of these regions is relatively small, which is in agreement with the XRR/NR measurements that do show a relatively modest roughness and a good fit, which should not be possible if the surface fraction of these regions is large. In addition, we do know from the XRR measurements of Figure S1 and the corresponding fitted SLD/atomic number density that the number of atoms per volume unit is unaffected by Fe substitution, suggesting that the $Ta_{1-y}Fe_y$ layers have a similar atomic density as the bcc Ta-phase.

Similar conclusions can be obtained for the substitution of Ta by Co (Figures S3, S4 and S5) or Ni (Figures S6, S7, and

https://doi.org/10.1021/acsomega.4c06955
ACS Omega 2024, 9, 41978−41989

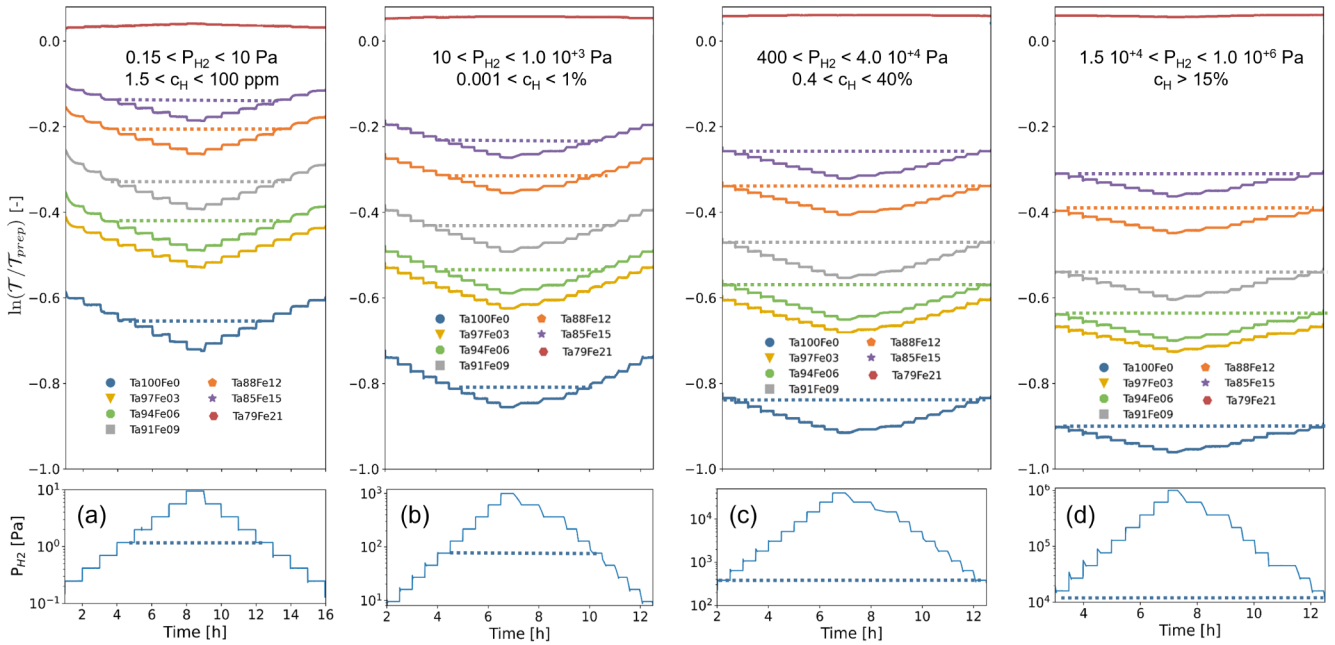

Figure 5. Changes of the green light optical transmission $\mathcal{T}$ of the 40 nm $Ta_{1-y}Fe_y$ thin film. All samples have a 4 nm Ti adhesion layer capped with a 10 nm $Pd_{0.60}Au_{0.35}Cu_{0.05}$ layer, the contribution of which was subtracted by subtracting the response of a non-hydrogenating 40 nm $Ta_{0.5}Pd_{0.5}$ with the same capping and adhesion layers. The film was exposed at T = 28 °C to various increasing and decreasing pressure steps of (a) $1.5 \times 10^{-1} \leq P_{H2} \leq 1.0 \times 10^{1}$ Pa, (b) $1.0 \times 10^{1} \leq P_{H2} \leq 1.0 \times 10^{3}$ Pa, (c) $4.0 \times 10^{2} \leq P_{H2} \leq 4.0 \times 10^{4}$ Pa, and (d) $1.5 \times 10^{4} \leq P_{H2} \leq 1.0 \times 10^{6}$ Pa. The dashed lines indicate levels of the same transmission (top panel) and pressure (bottom panel). The hydrogen concentrations indicated correspond to an environment with a total pressure of $P_{tot} = 10^5$ Pa.

S8). In both cases, the peak position is hardly affected by the substitution of Ta by the metal alloyant, while the peak intensity is sharply decreased until the point at y = 0.21 that no more bcc Ta peak can be observed. It suggests that as for the substitution of Ta by Fe, the substitution by Co or Ni results in the formation of another phase of which the fraction increases with increasing concentration of the alloyant.

3.1.2. In Situ Neutron Reflectometry. The amount of hydrogen absorbed and the expansion of the material when it absorbs hydrogen are two important quantities for a hydrogen sensing material. The absorption of hydrogen is directly related to the optical response of the hydrogen sensing material. As such, it should be within the pressure window of interest. Furthermore, a too large absorption of hydrogen may cause long response times as more hydrogen needs to be dissociated from molecular into atomic hydrogen and subsequently transported.[27,41] On the other hand, a too small absorption may not give a large optical contrast. In addition, too large absorption of hydrogen may cause a large expansion of the material, which can compromise its stability. As such, it is beneficial to be able to tune both the absolute amount of hydrogen absorbed and the pressure range in which the material absorbs hydrogen.

Neutron reflectometry is used to determine both the amount of hydrogen absorbed and the expansion for several compositions as a function of hydrogen pressure. The neutron reflectograms, collected for different compositions are presented in Figure 3. These neutron reflectograms are subsequently fitted to a model to obtain estimates of the thickness and scattering length density. From these quantities, the expansion and hydrogen concentration of the layer can be obtained (see Experimental Section for more details). We note that we did not observe substantial off-specular scattering, which indicates that within the coherence length of the neutron, no domains are formed with substantially different SLDs.

Figure 4 reports the hydrogen concentration and thickness expansion of the $Ta_{1-y}M_y$ layer. We can derive three important conclusions from the data. First, with increasing doping we observe a small decrease in the hydrogenation of the layer at a given hydrogen pressure of P_{H2} = 24600 Pa (cH_{H2} = 25% when measured at 1 atm) from $x \approx 0.6$ for TaH_x to $x \approx 0.4$ for $Ta_{0.79}M_{0.21}H_x$ [Figure 4a]. However, this decrease is much smaller than for Ru alloying, where a reduction to $x \approx 0.1$ was observed for $Ta_{0.79}M_{0.21}H_x$.[40] Correspondingly, we see only a small reduction of the expansion of the $Ta_{1-y}M_yH_x$ layer from about 8% for Ta to 5% for y = 0.21 [Figure 4b]. Second, we observe the same trends for substitution with Fe, Co, and Ni. Third, nonbcc $Ta_{1-y}M_y$ absorbs substantial amounts of hydrogen. Indeed, we observe a substantial hydrogenation of the $Ta_{0.79}M_{0.21}H_x$ layer to $x \approx 0.4$ [Figure 4a] while XRD did not show any reflection of a crystalline phase for this sample (Figure 2).

All these observations are consistent with the fact that substitution of Ta by either Fe, Co, and Ni hardly reduces the size of the (crystalline) unit cell, and therefore hardly the hydrogenation of the layer.[43,65] The small reduction observed may simply be the result of the fact that Fe, Co, or Ni atoms block the interstitial sites were hydrogen can be inserted in the bcc structure of Ta[42] or sites in the additional phase, or decreases the average distance between the atoms within the additional phase. This would then be similar to the case of doping Pd with, e.g., Au or Ag, alloyants that itself do not bond with hydrogen and thereby block sites where hydrogenation may occur.

https://doi.org/10.1021/acsomega.4c06955
ACS Omega 2024, 9, 41978−41989

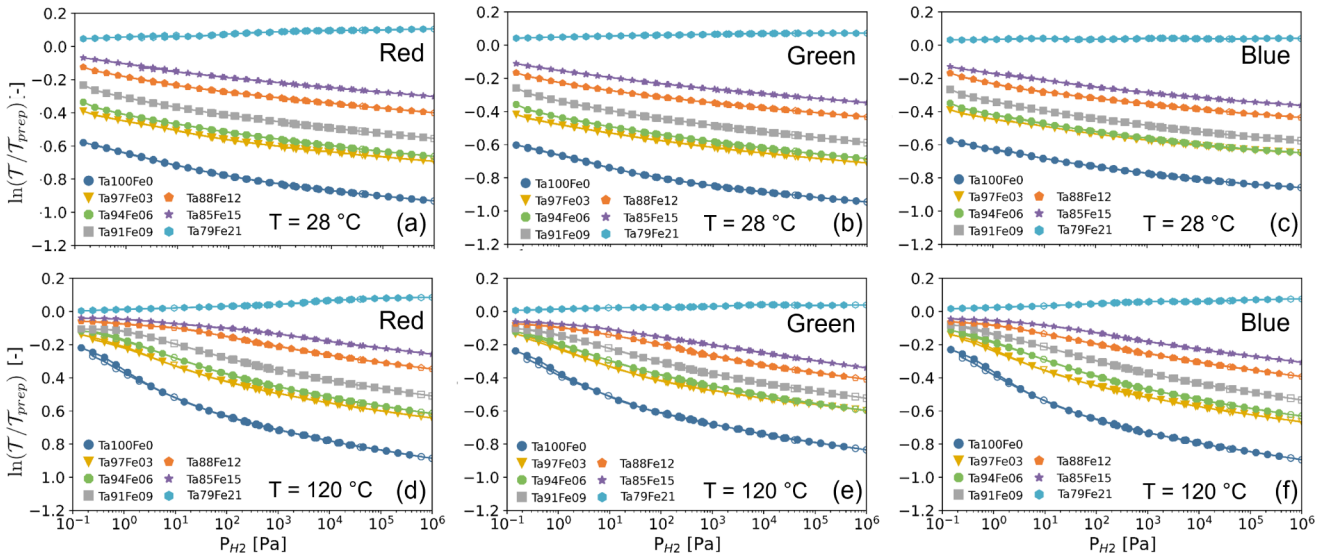

Figure 6. Partial hydrogen pressure dependence of the green light optical transmission $\mathcal{T}$ of 40 nm $Ta_{1-y}Fe_y$ sensing layers measured relative to the optical transmission of the as-prepared state ($\mathcal{T}_{prep}$) at (a−c) T = 28 °C and (d−f) T = 120 °C. Each data-point corresponds to the optical transmission after exposing the film for at least 30 min to a constant pressure of P_{H2} =10^{-1}−10^{6} Pa, where the closed data points correspond to increasing pressure steps, and the open points to decreasing pressure steps. The data in panels (a,d) correspond to the red, in panels (b,e) to the green, and in panels (c,f) to the blue spectrum (see Figure S10).

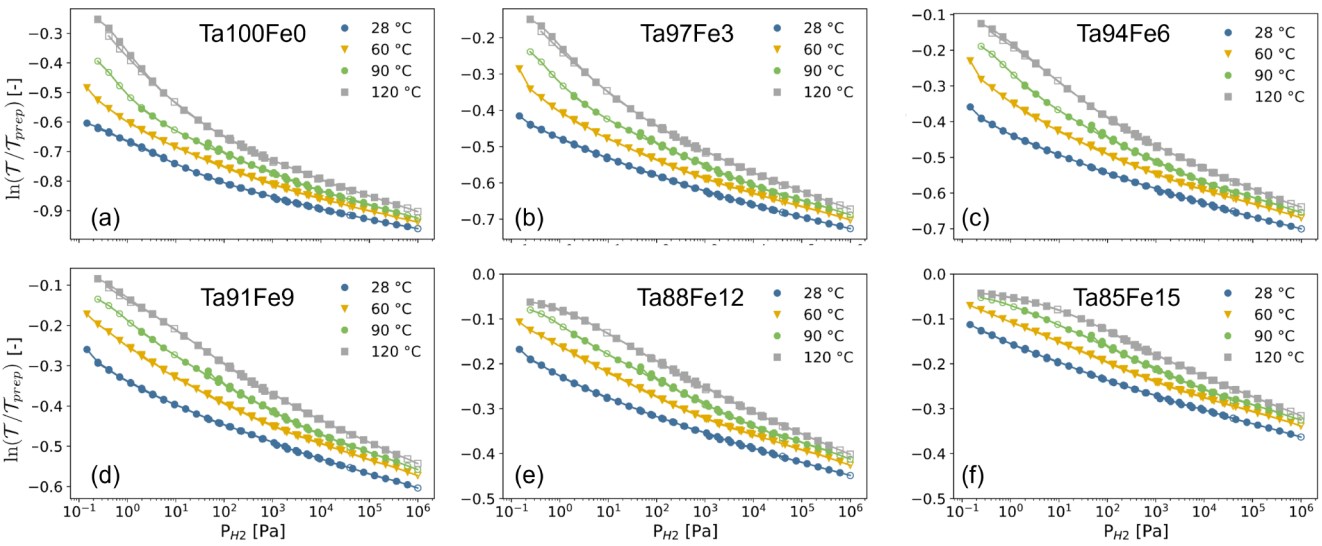

Figure 7. Partial hydrogen pressure and temperature dependence of the green light optical transmission $\mathcal{T}$ measured relative to the optical transmission of the as-prepared state ($\mathcal{T}_{prep}$) at T = 28 °C of the 40 nm $Ta_{1-y}Fe_y$ sensing layers with (a) y = 0, (b) y = 0.03, (c) y = 0.06, (d) y = 0.09, (e) y = 0.12, and (f) y = 0.15. Each data-point corresponds to the optical transmission after exposing the film for at least 30 min to a constant pressure of P_{H2} = 10^{-1} P_{H2} =10^{-1}−10^{6} Pa.

Despite that the maximum hydrogenation is not reduced substantially by alloying with Fe, Co, or Ni, there may still be an advantage if the partial hydrogen pressure dependence of the hydrogen content, i.e., the pressure composition isotherm, of the $Ta_{1-y}M_yH_x$ layer is affected. Indeed, the sensitivity/resolution of a hydrogen sensor is directly related to the derivative of the hydrogen content of the layer with respect to the partial hydrogen pressure. Here, we define the sensitivity/resolution as the accuracy with which one can determine the hydrogen pressure. Shifting the pressure composition isotherm thus changes the hydrogen pressure range of the sensing material, while a change in slope affects the resolution.

To study how alloying alters the pressure composition isotherm, we have, for the case of Ta, $Ta_{0.94}Fe_{0.06}$, $Ta_{0.88}Fe_{0.12}$, $Ta_{0.79}Fe_{0.21}$, $Ta_{0.94}Ni_{0.06}$, and $Ta_{0.79}Ni_{0.21}$, determined the partial hydrogen pressure dependence of the hydrogen concentration in these layers. These data are reported in Figures 4c and S15 and the slope of these curves is thus directly related to the resolution of the sensing material. Indeed, a steeper slope provides ceteris paribus a better resolution. On the other hand, if the slope is too steep, the sensing range may be compromised as the maximum hydrogen concentration in the material is reached within a smaller pressure window. Here, we observe with increasing partial hydrogen pressure a gradual increase in hydrogen concentration for all materials, which is

https://doi.org/10.1021/acsomega.4c06955
ACS Omega 2024, 9, 41978−41989

beneficial for hydrogen sensing with a constant resolution across a large pressure window. In addition, we observed a slight steepening of the slope with respect to Ta. This indicates that if the optical contrast changes induced by the absorption of hydrogen are similar for all materials, then the sensitivity/resolution can be increased.

3.2. Optical Response and Sensing Range. The X-ray diffraction and neutron reflectometry results indicate that phase coexistence occurs for $y > 0$ where the bcc-$Ta_{1-y}M_y$ phase coexists with another unidentified phase. The fraction of this unidentified phase increases with increasing doping, until for $y = 0.2$ no more crystalline bcc phase is present. At the same time, the sizes of the bcc-$Ta_{1-y}M_y$ unit cell are highly similar for all compounds. Furthermore, neutron reflectometry results indicate that the Fe substitution only slightly reduces the amount of hydrogen absorbed by the alloy and that all compositions gradually absorb hydrogen.

As a next step, we see how these structural properties are reflected in the optical ones and test whether the materials feature a monotonic, gradual change of the optical properties over a large range of partial hydrogen pressures (concentrations) without any dependence of the optical properties on the (pressure) history of the sensor, i.e., free of any hysteresis. To do this, we measure the changes of the optical transmission $\mathcal{T}$ relative to that of the as-prepared state $\mathcal{T}_{prep}$ when applying a series of increasing and decreasing partial hydrogen pressure steps at $T = 28$ °C. To change the partial hydrogen pressure, we varied the total pressures of 0.1%, 4%, and 100% of H_2 in Ar gas inside a temperature- and pressure-controlled cell. Figure 5 depicts the green-light optical transmissions for four different hydrogen pressure and concentration regions for the $Ta_{1-y}Fe_y$ compositions.

Figure 5 shows that for all compounds with $y \leq 0.15$ and for all four pressure regions, well-defined and stable levels of transmission are observed in response to a change in hydrogen pressure. With an increase in hydrogen pressure, the optical transmission decreases gradually but monotonically. Most importantly, the level of optical transmission is exactly the same for each pressure level after increasing and decreasing steps in hydrogen pressure. This implies that the response is completely free of any hysteresis across the entire hydrogen pressure range of $0.1 < P_{H2} < 10^6$ Pa.

Figure 6 summarizes the optical response across the entire pressure range measured of $1.0 \times 10^{-1} < P_{H2} < 10^6$ Pa, for various $Ta_{1-y}Fe_y$ compositions with $0.0 \leq y \leq 0.2$ at both room temperature and at $T = 120$ °C. Data for $Ta_{1-y}Co_y$ and $Ta_{1-y}Ni_y$ can be found in Figures S16 and S17, respectively, and data for additional temperatures in Figure 7. These figures display the pressure−transmission-isotherms (PTIs) of the sensing layers, for red, green, and blue lights, where each closed data-point corresponds to the optical transmission obtained after exposing the material for a minimum of 30 min to a constant hydrogen pressure after an increase in pressure, while the open points indicate the optical transmission deduced after decreasing stepwise the hydrogen pressure.

For the $Ta_{0.79}Fe_{0.21}$, $Ta_{0.79}Co_{0.21}$, and $Ta_{0.79}Ni_{0.21}$ films hardly any optical response can be discerned in the red, green, and blue spectra despite the fact that these films absorb considerable amounts of hydrogen (Figure 4): only a small increase of the red-light optical transmission is observed with increasing hydrogen concentration. It suggests that in this sample in which no more bcc phase is present, the absorption of hydrogen by the material hardly affects the optical properties of the material for the probed wavelengths, making it unsuitable for optical hydrogen sensing purposes.

For all $Ta_{1-y}Fe_y$, $Ta_{1-y}Co_y$ and $Ta_{1-y}Ni_y$ films with $y \leq 0.15$, the PTIs do indicate a gradual, monotonic decrease of the optical transmission over the entire sensing range of 7 orders of magnitude with no hysteresis. With increasing alloyant concentration, the absolute change of the optical response at a given pressure becomes smaller, but also its slope is slightly reduced (Figure S18). This is undesirable, as the slope of the optical read-out parameter, in this case $\ln(\mathcal{T}/\mathcal{T}_{ref})$, defines the accuracy with which one can deduce a hydrogen pressure (sensitivity/resolution). Although small, we do observe a slight shift of the pressure window, in which the contrast is provided. This becomes especially clear at elevated temperatures [Figure 6d−f].

To further analyze the sensitivity, one can consider the two contributions to the sensitivity: the change in the hydrogen concentration within the sensing material with a change in hydrogen pressure $\frac{dx}{dP_{H2}}$, and the amount by which the optical transmission changes in the material for every hydrogen atom absorbed $\frac{d(\ln(\mathcal{T}/\mathcal{T}_{ref}))}{dx}$. The sensitivity $\frac{d(\ln(\mathcal{T}/\mathcal{T}_{ref}))}{dP_{H2}}$ is then simply the product of these two terms:

$$\frac{\mathrm{d}(\ln(\mathcal{T}/\mathcal{T}_{ref}))}{\mathrm{d}P_{H_2}} = \frac{d(\ln(\mathcal{T}/\mathcal{T}_{ref}))}{dx}\frac{dx}{\mathrm{d}P_{H_2}} \quad (3)$$

We first consider the second term, $\frac{dx}{dP_{H2}}$ by revisiting the neutron reflectometry results of Figure 4c. In this figure, the slope equals $\frac{dx}{dP_{H2}}$, and this slope is larger for $Ta_{0.94}Fe_{0.06}$ and $Ta_{0.88}Fe_{0.12}$ than it is for Ta. On the basis of these results, one would thus expect a larger sensitivity for all these materials as compared to tantalum. However, this is not observed. This implies that the other contribution to the sensitivity, $\frac{d(\ln(\mathcal{T}/\mathcal{T}_{ref}))}{dx}$, should thus be reduced with Fe substitution.

To deduce how $\frac{d(\ln(\mathcal{T}/\mathcal{T}_{ref}))}{dx}$ changes with Fe substitution, we plot in Figure 8 the changes of the green-light optical transmission $\ln(\mathcal{T}/\mathcal{T}_{ref})$ as a function of the hydrogen concentration in the $Ta_{1-y}Fe_yH_x$ layer. To construct this plot, we have matched for every partial hydrogen pressure measured with neutron reflectometry in Figure 4c the obtained hydrogen concentration in the $Ta_{1-y}Fe_yH_x$ layer with the value

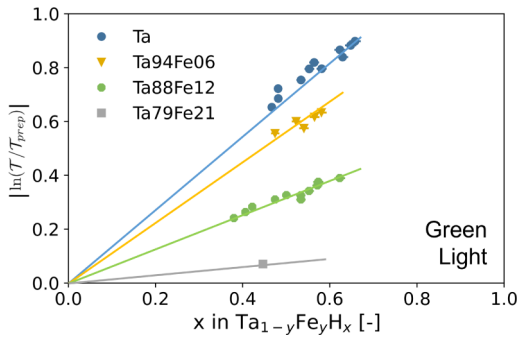

Figure 8. Relation between the hydrogen-to-metal ratio x and the absolute changes of the green-light optical transmission relative to the as-prepared state $\mathcal{T}_{prep}$ of the $Ta_{1-y}Fe_yH_x$ layer. The lines serve as guides for the eyes.

https://doi.org/10.1021/acsomega.4c06955
ACS Omega 2024, 9, 41978−41989

of $\ln(\mathcal{T}/\mathcal{T}_{ref})$ at exactly the same partial hydrogen pressure from Figure 6.

Similar to reports for other metal hydrides,[25,28,31,37,40,66] we observe a linear relationship between the amount of hydrogen absorbed by the $Ta_{1-y}Fe_yH_x$ layer and the optical contrast for all three compositions. In fact, such a scaling is not trivial at all for solid solutions, intermetallic compounds, or amorphous materials. Indeed, this would imply that the effect on the optical properties of absorbing hydrogen is completely independent of the hydrogen concentration within the solid solution and only affected by the composition of the host metal lattice.[10]

The most important message of Figure 8 is that with increasing Fe concentration, the slope $\frac{d(\ln(\mathcal{T}/\mathcal{T}_{ref}))}{dx}$ decreases substantially. In other words, doping with Fe has a negative influence on the sensitivity of the hydrogen sensing material. $\frac{d(\ln(\mathcal{T}/\mathcal{T}_{ref}))}{dx}$ decreases from $\frac{d(\ln(\mathcal{T}/\mathcal{T}_{ref}))}{dx} \approx 1$ for Ta to $\frac{d(\ln(\mathcal{T}/\mathcal{T}_{ref}))}{dx} \approx 0.4$ for $Ta_{0.88}Fe_{0.12}$. Said differently, the absorption of the same amount of hydrogen results in a lower optical contrast. This explains why the sensitivity of the hydrogen sensing material drops with increasing alloyant concentration, while a similar hydrogenation is observed.

The decrease of $\frac{d(\ln(\mathcal{T}/\mathcal{T}_{ref}))}{dx}$ with Fe doping is unwanted. In the ideal world, one would have an as high as possible value of $\frac{d(\ln(\mathcal{T}/\mathcal{T}_{ref}))}{dx}$ as different from $\frac{dx}{dP_{H2}}$ it has no negative side effects, such as potentially longer response times owing to more hydrogen that needs to be dissociated/transported, or possibly a reduced mechanical stability owing to a larger volumetric expansion.

The facts that the optical contrast is reduced with increasing concentration of the alloyant, that the reduction of the hydrogen concentration in the materials with increasing alloyant is relatively small, and that alloying only causes a small shift of the pressure range of the material shows that the ability to tune the sensing properties of Ta by alloying with Fe, Co, or Ni is limited, especially compared to alloying with Pd[38] or Ru.[40] Nevertheless, thin film $Ta_{1-y}Fe_y$, $Ta_{1-y}Co_y$, and $Ta_{1-y}Ni_y$ do show favorable hydrogen sensing properties for $y \lesssim 0.15$ with a pressure range of 7 orders of magnitude that is stable and completely free of any hysteresis.

4. CONCLUSION

In conclusion, we have studied the structural and optical properties of tantalum−iron, tantalum−cobalt, and tantalum−nickel sputtered thin films both ex situ and while being exposed to various hydrogen pressures/concentrations with a focus on optical hydrogen sensing applications. While the idea was to reduce the unit cell size by doping Ta with a smaller element to shift the pressure composition isotherms to higher pressures, X-ray diffraction measurements indicate for all three alloyants little to no lattice compression but the coexistence of a crystalline bcc phase and another unidentified phase, that could, for example, be an amorphous phase or intermetallic compound. The fraction of this unidentified phase increases with increasing alloyant concentrations and at $y = 0.2$ only an amorphous phase is observed. Neutron reflectometry indicates that no large reduction in hydrogen concentration is observed at a given hydrogen pressure and that also the sample without any bcc phase absorbs considerable amounts of hydrogen (H/M > 0.5). Despite the phase coexistence, optical measurements indicate a gradual hydrogenation of the materials with increasing hydrogen pressure/concentration, ensuring a sensing range of over 7 orders of magnitude in pressure up to 15% alloyant concentration, while hardly any optical response is observed for the samples that have no bcc phase. As such, this makes the materials applicable to hydrogen sensing applications. However, the ability to tune the sensing properties of Ta with Fe, Co, or Ni is relatively small and provides less flexibility than substitution with earlier considered Pd or Ru.

■ ASSOCIATED CONTENT

Supporting Information

The Supporting Information is available free of charge at https://pubs.acs.org/doi/10.1021/acsomega.4c06955.

Table with deposition conditions, spectrum of the LED lights used for the optical measurements, spectral sensitivity of the three color channels of the camera used for the optical measurements, X-ray diffraction (XRD) measurements of the films before and after exposure to hydrogen, in situ NR results of $Ta_{1-y}Ni_y$ films, optical response to hydrogen of $Ta_{1-y}Co_y$ and $Ta_{1-y}Ni_y$, optical sensitivity of the $Ta_{1-y}Fe_y$ films (PDF)

■ AUTHOR INFORMATION

Corresponding Author

Lars J. Bannenberg − *Faculty of Applied Sciences, Delft University of Technology, JB Delft 2629, The Netherlands;* orcid.org/0000-0001-8150-3694; Email: l.j.bannenberg@tudelft.nl

Authors

Isa M. Veeneman − *Faculty of Applied Sciences, Delft University of Technology, JB Delft 2629, The Netherlands*

Folkert I. B. Straus − *Faculty of Applied Sciences, Delft University of Technology, JB Delft 2629, The Netherlands*

Hsin-Yu Chen − *Faculty of Applied Sciences, Delft University of Technology, JB Delft 2629, The Netherlands*

Christy J. Kinane − *ISIS Neutron Source, Rutherford Appleton Laboratory, Didcot OX11 0S8X, United Kingdom;* orcid.org/0000-0002-1185-0719

Stephen Hall − *ISIS Neutron Source, Rutherford Appleton Laboratory, Didcot OX11 0S8X, United Kingdom;* orcid.org/0000-0003-0753-5123

Michel A. Thijs − *Faculty of Applied Sciences, Delft University of Technology, JB Delft 2629, The Netherlands*

Herman Schreuders − *Faculty of Applied Sciences, Delft University of Technology, JB Delft 2629, The Netherlands*

Complete contact information is available at: https://pubs.acs.org/10.1021/acsomega.4c06955

Notes

The authors declare the following competing financial interest(s): Two of the authors are listed as inventor on a patent for these materials owned by Delft University of Technology entitled: Optical Thin-Film Hydrogen Sensing Material Based on Tantalum or Other Group V Element Alloy.

■ ACKNOWLEDGMENTS

We warmly thank Kees de Vroege, Raymon Bresser, and Piet van der Ende for their support with the neutron reflectometry

measurements and Bart Boshuizen with designing and maintaining Labview software to control the pressure cells. Marcel Bus is thanked for the AFM measurements. Erwin Janssen and Jörg Haberlah are thanked for providing the gas cylinders. Support at ISIS from Andy Church, Tom Charleston, Chris Goodway, and Jason Chandler is greatly appreciated. The experiments at the ISIS Pulsed Neutron and Muon Source were supported by a beamtime allocation from the Science and Technology Facilities Council (RB 2210119). The neutron reflectometry data collected at the ISIS Neutron Source is available at: 10.5286/ISIS.E.RB2210119.

REFERENCES

(1) Brandon, N. P.; Kurban, Z. Clean Energy and the Hydrogen Economy. *Philos. Trans. R. Soc., A* **2017**, *375*, 20160400.
(2) Editorial Hydrogen to the Rescue. *Nat. Mater.*, **2018**, *565*. DOI: 10.1038/s41563-018-0129-y.
(3) Abe, J. O.; Popoola, A. P. I.; Ajenifuja, E.; Popoola, O. M. Hydrogen Energy, Economy and Storage: Review and Recommendation. *Int. J. Hydrogen Energy* **2019**, *44*, 15072−15086.
(4) Glenk, G.; Reichelstein, S. Economics of Converting Renewable Power to Hydrogen. *Nat. Energy* **2019**, *4*, 216−222.
(5) Bakenne, A.; Nuttall, W.; Kazantzis, N. Sankey-Diagram-based Insights into the Hydrogen Economy of Today. *Int. J. Hydrogen Energy* **2016**, *41*, 7744−7753.
(6) El Kharbachi, A.; Dematteis, E. M.; Shinzato, K.; Stevenson, S. C.; Bannenberg, L. J.; Heere, M.; Zlotea, C.; Szilágyi, P. A.; Bonnet, J.-P.; Grochala, W.; et al. Metal Hydrides and Related Materials. Energy Carriers for Novel Hydrogen and Electrochemical Storage. *J. Phys. Chem. C* **2020**, *124*, 7599−7607.
(7) Warwick, N.; Griffiths, P.; Keeble, J.; Archibald, A.; Pyle, J.; Shine, K. Atmospheric implications of increased Hydrogen use. *Policy Pap.* **2022**, 75.
(8) Hübert, T.; Boon-Brett, L.; Black, G.; Banach, U. Hydrogen Sensors−a Review. *Sens. Actuators, B* **2011**, *157*, 329−352.
(9) Wadell, C.; Syrenova, S.; Langhammer, C. Plasmonic Hydrogen Sensing with Nanostructured Metal Hydrides. *ACS Nano* **2014**, *8*, 11925−11940.
(10) Bannenberg, L. J.; Boelsma, C.; Asano, K.; Schreuders, H.; Dam, B. Metal Hydride Based Optical Hydrogen Sensors. *J. Phys. Soc. Jpn.* **2020**, *89*, 051003.
(11) Bannenberg, L. J.; Heere, M.; Benzidi, H.; Montero, J.; Dematteis, E. M.; Suwarno, S.; Jaron, T.; Winny, M.; Orlowski, P. A.; Wegner, W.; et al. Metal (boro-) Hydrides for High Energy Density Storage and Relevant Emerging Technologies. *Int. J. Hydrogen Energy* **2020**, *45* (58), 33687−33730.
(12) Darmadi, I.; Nugroho, F. A. A.; Langhammer, C. High-Performance Nanostructured Palladium-Based Hydrogen Sensors−Current Limitations and Strategies for Their Mitigation. *ACS Sens.* **2020**, *5*, 3306−3327.
(13) Koo, W.-T.; Cho, H.-J.; Kim, D.-H.; Kim, Y. H.; Shin, H.; Penner, R. M.; Kim, I.-D. Chemiresistive Hydrogen Sensors: Fundamentals, Recent Advances, and Challenges. *ACS Nano* **2020**, *14*, 14284−14322.
(14) Chen, K.; Yuan, D.; Zhao, Y. Review of Optical Hydrogen Sensors Based on Metal Hydrides: Recent Developments and Challenges. *Opt Laser Technol.* **2021**, *137*, 106808.
(15) Flanagan, T. B.; Clewley, J. D. Hysteresis in metal hydrides. *J. Less-Common Met.* **1982**, *83*, 127−141.
(16) Qian, S.; Northwood, D. O. Hysteresis in metal-hydrogen systems: a critical review of the experimental observations and theoretical models. *Int. J. Hydrogen Energy* **1988**, *13*, 25−35.
(17) Balasubramaniam, R. Hysteresis in metal−hydrogen systems. *J. Alloys Compd.* **1997**, *253*, 203−206.
(18) Cappillino, P. J.; Lavernia, E. J.; Ong, M. D.; Wolfer, W. G.; Yang, N. Y. Plastic deformation and hysteresis for hydrogen storage in Pd−Rh alloys. *J. Alloys Compd.* **2014**, *586*, 59−65.
(19) Pivak, Y.; Schreuders, H.; Slaman, M.; Griessen, R.; Dam, B. Thermodynamics, Stress Release and Hysteresis Behavior in Highly Adhesive Pd−H Films. *Int. J. Hydrogen Energy* **2011**, *36*, 4056−4067.
(20) Butler, M. A. Fiber optic sensor for hydrogen concentrations near the explosive limit. *J. Electrochem. Soc.* **1991**, *138*, L46−L47.
(21) Butler, M. A. Micromirror optical-fiber hydrogen sensor. *Sens. Actuators, B* **1994**, *22*, 155−163.
(22) Zhao, Z.; Carpenter, M. A.; Xia, H.; Welch, D. All-optical hydrogen sensor based on a high alloy content palladium thin film. *Sens. Actuators, B* **2006**, *113*, 532−538.
(23) Westerwaal, R. J.; Rooijmans, J. S. A.; Leclercq, L.; Gheorghe, D. G.; Radeva, T.; Mooij, L.; Mak, T.; Polak, L.; Slaman, M.; Dam, B.; et al. Nanostructured Pd-Au Based Fiber Optic Sensors for Probing Hydrogen Concentrations in Gas Mixtures. *Int. J. Hydrogen Energy* **2013**, *38*, 4201−4212.
(24) Wadell, C.; Nugroho, F. A. A.; Lidstrom, E.; Iandolo, B.; Wagner, J. B.; Langhammer, C. Hysteresis-Free Nanoplasmonic Pd−Au Alloy Hydrogen Sensors. *Nano Lett.* **2015**, *15*, 3563−3570.
(25) Nugroho, F. A. A.; Darmadi, I.; Zhdanov, V. P.; Langhammer, C. Universal Scaling and Design Rules of Hydrogen Induced Optical Properties in Pd and Pd-Alloy Nanoparticles. *ACS Nano* **2018**, *12*, 9903−9912.
(26) Darmadi, I.; Nugroho, F. A. A.; Kadkhodazadeh, S.; Wagner, J. B.; Langhammer, C. Rationally Designed PdAuCu Ternary Alloy Nanoparticles for Intrinsically Deactivation-Resistant Ultrafast Plasmonic Hydrogen Sensing. *ACS Sens.* **2019**, *4*, 1424−1432.
(27) Nugroho, F. A. A.; Darmadi, I.; Cusinato, L.; Susarrey-Arce, A.; Schreuders, H.; Bannenberg, L. J.; Bastos da Silva Fanta, A.; Kadkhodazadeh, S.; Wagner, J. B.; Antosiewicz, T. J.; et al. Metal−polymer hybrid nanomaterials for plasmonic ultrafast hydrogen detection. *Nat. Mater.* **2019**, *18* (5), 489−495.
(28) Bannenberg, L. J.; Nugroho, F. A. A.; Schreuders, H.; Norder, B.; Trinh, T. T.; Steinke, N.-J.; Van Well, A. A.; Langhammer, C.; Dam, B. Direct Comparison of PdAu Alloy Thin Films and Nanoparticles upon Hydrogen Exposure. *ACS Appl. Mater. Interfaces* **2019**, *11*, 15489−15497.
(29) Palm, K. J.; Murray, J. B.; McClure, J. P.; Leite, M. S.; Munday, J. N. In Situ Optical and Stress Characterization of Alloyed Pd_xAu_{1-x} Hydrides. *ACS Appl. Mater. Interfaces* **2019**, *11*, 45057−45067.
(30) Nugroho, F. A. A.; Bai, P.; Darmadi, I.; Castellanos, G. W.; Fritzsche, J.; Langhammer, C.; Gómez Rivas, J.; Baldi, A. Inverse designed plasmonic metasurface with parts per billion optical hydrogen detection. *Nat. Commun.* **2022**, *13* (1), 5737.
(31) Boelsma, C.; Bannenberg, L. J.; van Setten, M. J.; Steinke, N.-J.; Van Well, A. A.; Dam, B. Hafnium—an optical hydrogen sensor spanning six orders in pressure. *Nat. Commun.* **2017**, *8* (1), 15718.
(32) Bannenberg, L. J.; Schreuders, H.; Kim, H.; Sakaki, K.; Hayashi, S.; Ikeda, K.; Otomo, T.; Asano, K.; Dam, B. Suppression of the Phase Coexistence of the fcc−fct Transition in Hafnium-Hydride Thin Films. *J. Phys. Chem. Lett.* **2021**, *12*, 10969−10974.
(33) Isidorsson, J.; Giebels, I.; Griessen, R.; Di Vece, M. Tunable reflectance Mg−Ni−H films. *Appl. Phys. Lett.* **2002**, *80*, 2305−2307.
(34) Bao, S.; Tajima, K.; Yamada, Y.; Okada, M.; Yoshimura, K. Magnesium−titanium alloy thin-film switchable mirrors. *Sol. Energy Mater. Sol. Cells* **2008**, *92*, 224−227.
(35) Slaman, M.; Dam, B.; Pasturel, M.; Borsa, D. M.; Schreuders, H.; Rector, J.; Griessen, R. Fiber Optic Hydrogen Detectors Containing Mg-Based Metal Hydrides. *Sens. Actuators, B* **2007**, *123*, 538−545.
(36) Palm, K. J.; Karahadian, M. E.; Leite, M. S.; Munday, J. N. Optical Tunability and Characterization of Mg−Al, Mg−Ti, and Mg−Ni Alloy Hydrides for Dynamic Color Switching Devices. *ACS Appl. Mater. Interfaces* **2023**, *15*, 1010−1020.
(37) Bannenberg, L. J.; Boelsma, C.; Schreuders, H.; Francke, S.; Steinke, N.-J.; Van Well, A. A.; Dam, B. Optical Hydrogen Sensing Beyond Palladium: Hafnium and Tantalum as Effective Sensing Materials. *Sens. Actuators, B* **2019**, *283*, 538−548.
(38) Bannenberg, L.; Schreuders, H.; Dam, B. Tantalum-Palladium: Hysteresis-Free Optical Hydrogen Sensor over 7 Orders of Magnitude

in Pressure with Sub-Second Response. *Adv. Funct. Mater.* **2021**, *31* (16), 2010483.
(39) Bannenberg, L. J.; Blom, L.; Sakaki, K.; Asano, K.; Schreuders, H. Completely elastic deformation of hydrogenated Ta thin films. *ACS Mater. Lett.* **2023**, *5*, 962−969.
(40) Bannenberg, L. J.; Schreuders, H.; van Beugen, N.; Kinane, C.; Hall, S.; Dam, B. Tuning the properties of thin film TaRu for hydrogen sensing applications. *ACS Appl. Mater. Interfaces* **2023**, *15*, 8033−8045.
(41) Bannenberg, L. J.; Boshuizen, B.; Ardy Nugroho, F. A.; Schreuders, H. Hydrogenation kinetics of metal hydride catalytic layers. *ACS Appl. Mater. Interfaces* **2021**, *13*, 52530−52541.
(42) San-Martin, A.; Manchester, F. D. The H-Ta (Hydrogen-Tantalum) System. *J. Phase Equilib.* **1991**, *12*, 332−343.
(43) Griessen, R.; Feenstra, R. Volume changes during hydrogen absorption in metals. *J. Phys. F: Met. Phys.* **1985**, *15*, 1013−1019.
(44) Hansen, M.; Anderko, K.; Salzberg, H. W. Constitution of binary alloys. *J. Electrochem. Soc.* **1958**, *105*, 260C.
(45) Jones, R. H.; Zackay, V. F.; Parker, E. R. Laves phase precipitation in Fe-Ta alloys. *Metall. Mater. Trans. B* **1972**, *3*, 2835−2842.
(46) Srikanth, S.; Petric, A. Optimization and calculation of the Fe-Ta phase diagram. *J. Alloys Compd.* **1994**, *203*, 281−288.
(47) Okamoto, H. Fe-Ta (iron-tantalum). *J. Phase Equilib. Diffus.* **2013**, *34*, 165−166.
(48) Okamoto, H. Co-Ta (cobalt-tantalum). *J. Phase Equilib. Diffus.* **2004**, *25* (6), 571.
(49) Shinagawa, K.; Chinen, H.; Omori, T.; Oikawa, K.; Ohnuma, I.; Ishida, K.; Kainuma, R. Phase equilibria and thermodynamic calculation of the Co−Ta binary system. *Intermetallics* **2014**, *49*, 87−97.
(50) Nash, A.; Nash, P. The Ni- Ta (nickel- tantalum) system. *Bull. Alloy Phase Diagrams* **1984**, *5*, 259−265.
(51) Okamoto, H. Ni-Ta (nickel-tantalum). *J. Phase Equilib. Diffus.* **2000**, *21*, 497.
(52) Chen, G. S.; Chen, S. T.; Huang, S. C.; Lee, H. Y. Growth mechanism of sputter deposited Ta and Ta−N thin films induced by an underlying titanium layer and varying nitrogen flow rates. *Appl. Surf. Sci.* **2001**, *169*, 353−357.
(53) Zhou, Y. M.; Xie, Z.; Xiao, H. N.; Hu, P. F.; He, J. Effects of deposition parameters on tantalum films deposited by direct current magnetron sputtering. *J. Vac. Sci. Technol., A* **2009**, *27*, 109−113.
(54) Bernoulli, D.; Müller, U.; Schwarzenberger, M.; Hauert, R.; Spolenak, R. Magnetron sputter deposited tantalum and tantalum nitride thin films: An analysis of phase, hardness and composition. *Thin Solid Films* **2013**, *548*, 157−161.
(55) Nasakina, E. O.; Sevostyanov, M. A.; Mikhaylova, A. B.; Baikin, A. S.; Sergienko, K. V.; Leonov, A. V.; Kolmakov, A. G. Formation of alpha and beta tantalum at the variation of magnetron sputtering conditions. *IOP Conf. Ser.: Mater. Sci. Eng.* **2016**, *110*, 012042.
(56) Bannenberg, L. J.; Verhoeff, D. J.; Jonckers Newton, N.; Thijs, M.; Schreuders, H. Thin film tetragonal beta-Ta for optical hydrogen sensing applications. *ACS Applied Nano Materials* **2024**, *7* (2), 1757.
(57) Björck, M.; Andersson, G. GenX: an Extensible X-ray Reflectivity Refinement Program Utilizing Differential Evolution. *J. Appl. Crystallogr.* **2007**, *40*, 1174−1178.
(58) Dalgliesh, R. M.; Langridge, S.; Plomp, J.; De Haan, V. O.; Van Well, A. A. Offspec, the ISIS spin-echo reflectometer. *Phys. B* **2011**, *406*, 2346−2349.
(59) Bannenberg, L. J.; van Exter, M.; Verleg, M. N.; Boshuizen, B.; Parnell, S. R.; Thijs, M.; Schreuders, H. Versatile pressure and temperature controlled cell for neutron reflectometry and small-angle neutron scattering. *J. Neutron Res.* **2024**, *26*, 1−13.
(60) Glavic, A.; Björck, M. GenX 3: the latest generation of an established tool. *J. Appl. Crystallogr.* **2022**, *55*, 1063−1071.
(61) Sears, V. F. Neutron scattering lengths and cross sections. *Neutron News* **1992**, *3*, 26−37.
(62) Bannenberg, L. J.; Schreuders, H.; van Eijck, L.; Heringa, J. R.; Steinke, N.-J.; Dalgliesh, R.; Dam, B.; Mulder, F. M.; van Well, A. A. Impact of Nanostructuring on the Phase Behavior of Insertion Materials: The Hydrogenation Kinetics of a Magnesium Thin Film. *J. Phys. Chem. C* **2016**, *120*, 10185−10191.
(63) Gremaud, R.; Broedersz, C. P.; Borsa, D. M.; Borgschulte, A.; Mauron, P.; Schreuders, H.; Rector, J. H.; Dam, B.; Griessen, R. Hydrogenography: An Optical Combinatorial Method To Find New Light-Weight Hydrogen-Storage Materials. *Adv. Mater.* **2007**, *19*, 2813−2817.
(64) Pivak, Y.; Gremaud, R.; Gross, K.; Gonzalez-Silveira, M.; Walton, A.; Book, D.; Schreuders, H.; Dam, B.; Griessen, R. Effect of the Substrate on the Thermodynamic Properties of PdH_x Films Studied by Hydrogenography. *Scr. Mater.* **2009**, *60*, 348−351.
(65) Brodowsky, H. On the non-ideal solution behavior of hydrogen in metals. *Ber. Bunsengesellschaft Phys. Chem.* **1972**, *76*, 740−746.
(66) Prinz, J.; Pálsson, G. K.; Korelis, P. T.; Hjörvarsson, B. Combined light and electron scattering for exploring hydrogen in thin metallic films. *Appl. Phys. Lett.* **2010**, *97*, 251910.

https://doi.org/10.1021/acsomega.4c06955
ACS Omega 2024, 9, 41978−41989